Camera Modeling, Centroiding Performance, and Geometric Camera Calibration on ASTERIA

Christopher M. Pong
Jet Propulsion Laboratory
California Institute of Technology
4800 Oak Grove Drive
Pasadena, CA 91109
818-354-5992
christopher.m.pong@jpl.nasa.gov

Matthew W. Smith
Jet Propulsion Laboratory
California Institute of Technology
4800 Oak Grove Drive
Pasadena, CA 91109
818-354-1319
matthew.w.smith@jpl.nasa.gov

***Abstract*—The Arcsecond Space Telescope Enabling Research in Astrophysics (ASTERIA) is a 10-kg, 6U CubeSat in low-Earth orbit that was able to achieve subarcsecond pointing stability and repeatability. To date, this is the best pointing on a spacecraft of its size. This paper will analyze various aspects of the performance of its key piece of hardware—the payload. First, a model of the optics and imager, which is used to simulate stellar images, will be presented. The imager parameters used in this model were derived from simple ground measurements. Next, a centroiding algorithm is provided and used on the simulated images to predict centroiding performance. These results will be shown to match on-orbit telemetry of centroiding performance, validating the modeling approach. This paper will then describe an approach for and results of a geometric camera calibration algorithm to estimate the focal length, distortion, and alignment parameters. The modeling, analyses, and results presented in this paper provide key information that can be used in a time-domain pointing simulation or a frequency-domain pointing error analysis.**

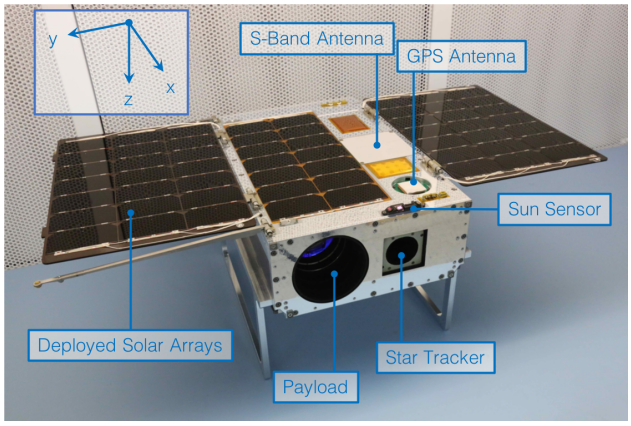

Figure 1: **ASTERIA with deployed solar arrays.**

TABLE OF CONTENTS

1. BACKGROUND & MOTIVATION

The Arcsecond Space Telescope Enabling Research in Astrophysics (ASTERIA) was the first CubeSat designed and integrated by the Jet Propulsion Laboratory (JPL) to have been successfully operated in space. This project actually traces its roots back to the ExoplanetSat project, led by the Massachusetts Institute of Technology [1–9]. ASTERIA is a 10-kg, 6U CubeSat that was deployed from the International Space Station on 20 November 2017 with a 400-km altitude and 51.6-deg inclination. Fig. 1 shows the completed flight vehicle and points out a few externally visible components. See [10] for more general information about the spacecraft and its operation.

The underlying goal of the mission is to image and perform photometry on bright, nearby stars and detect transiting exoplanets orbiting these stars. As a technology demonstration with an eye to enable this science, the payload pointing must be stable over an observation and repeatable across multiple observations. A two-stage control system was employed to achieve this pointing. Reaction wheels control the attitude of the spacecraft bus while a piezo stage translates the focal plane array to control the pointing of the payload. Fig. 2 shows a cartoon of how this two-stage control system functions. ASTERIA was actually able to achieve a pointing stability of 0.5 arcsec RMS over 20 minutes and a pointing repeatability of 1 mas RMS from observation to observation. See [11] for more information about the on-orbit performance of the attitude and pointing control subsystems.

One of the key aspects of understanding how ASTERIA was able to achieve this pointing is by analyzing the performance of its main sensor—the payload. Fig. 3 shows the flight payload and its components including the lens assembly, piezo stage, and imager. The lenses, lens rings, lens housing, bipods, baffle, mounting plates, and enclosure were all designed and integrated at JPL. The piezo stage is a Physik Instrumente P-733K110, which is a customized version of the off-the-shelf P-733.2CD. The electronics to control the piezo stage were designed and integrated at JPL. Attached to the piezo stage is a Fairchild Imaging CIS2521F0111 frontside-illuminated, monochrome CMOS image sensor. The electronics and harnessing to drive the imager were designed and integrated by Ecliptic Enterprises Corporation. The firmware to control the imager was developed by JPL.

A cartoon of a typical observation campaign is shown in Fig. 4. During orbit day, the spacecraft points its solar arrays at the Sun to charge its batteries. If there is a communication pass, the spacecraft will slew to point one of its antennas to the ground station. To perform an observation, the spacecraft

978-1-5386-6854-2/19/$31.00 © 2019 IEEE

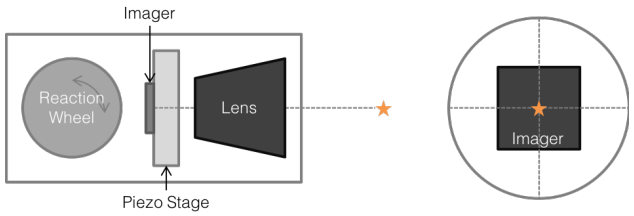

(a) Reaction wheels point the payload to the target star.

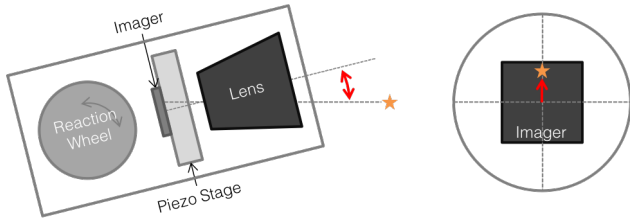

(b) Attitude errors cause the target star to shift on the imager.

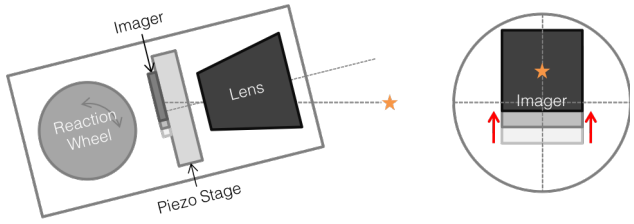

(c) Piezo stage shifts the imager to compensate for attitude errors.

Figure 2: **Two-stage pointing control concept.**

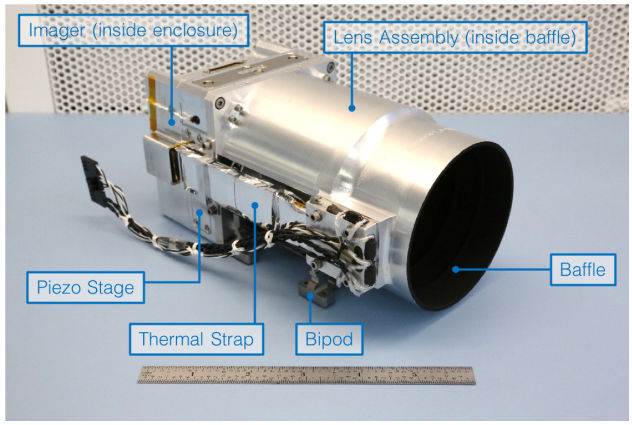

Figure 3: **ASTERIA payload.**

will slew to point to a star field, observe the star field normally during orbit night, and slew back to the Sun when the observation is complete.

To go into a little more detail on an observation, after the spacecraft slews to the desired star field, the payload is initialized. At this point, the payload starts taking up to eight windowed images at 20 Hz, with each window containing a single guide star, as seen in Fig. 5. For this to occur, the payload camera parameters such as focal length, distortion, and alignment with respect to the star tracker must have been calibrated properly, allowing the locations of each window to be selected such that the guide stars land within them upon completion of the slew to the star field. This concept of

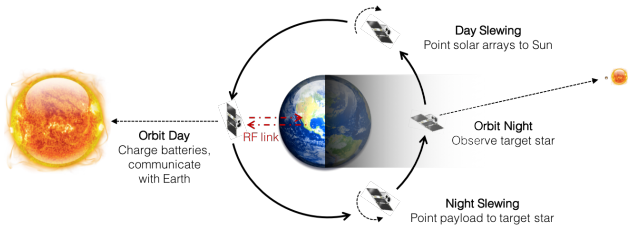

Figure 4: **ASTERIA concept of operations of a typical observation.**

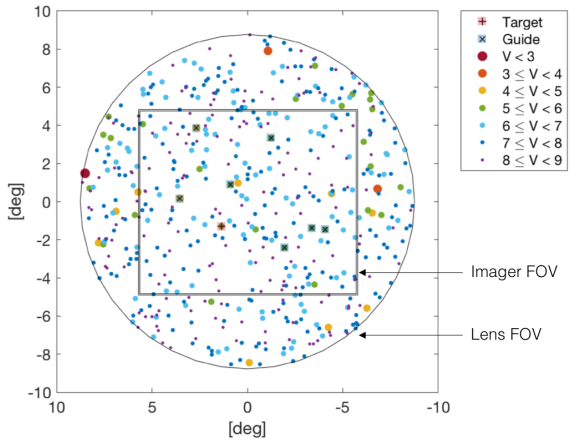

Figure 5: **Example of target and guide star windows for a star field around HD 219134.**

operations greatly simplifies the on-board software since it eliminates the need for full-frame image processing and star identification. These windowed images are then fed into the pointing control algorithms, which centroid the guide stars and use this information to compute a piezo stage command to control the payload pointing. Since the guide star centroids are the main source of feedback for the control algorithms, the amount of noise on these centroids is a significant term in the overall pointing error budget.

The focus of this paper is on the geometric camera calibration, centroiding performance, and modeling necessary to understand and analyze these two important aspects of the payload.

This paper will first introduce a camera model that can be used to simulate the camera functionality and performance. This model is split into two separate submodels. The first is a geometric camera model, which determines the location of stars on the imager given the spacecraft attitude. The second is an imager model, which produces simulated stellar images. Lab measurements will be described, which were used to extract some of the imager noise parameters used in the model. Simulated images will be compared against on-orbit images of actual stars, showing that the simulation produces realistic images with representative amounts of signal and noise.

The paper will then describe the centroiding algorithm used in the on-board pointing control software. Simulated images are run through this algorithm and the centroiding performance will be compared against on-orbit centroiding measurements, validating the camera model at a high level.

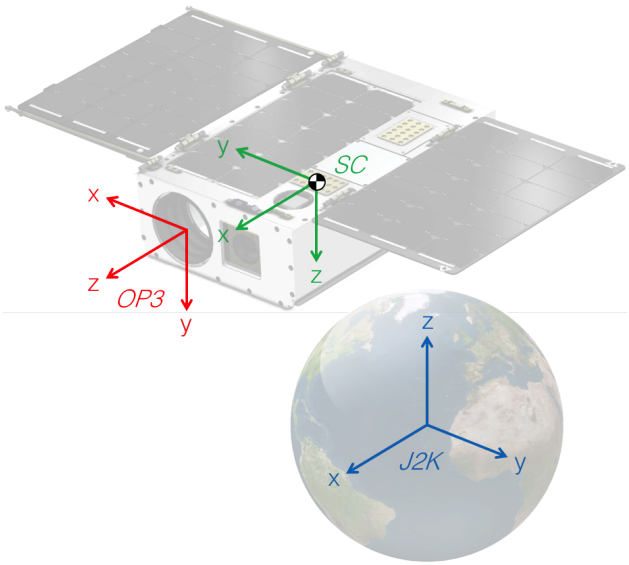

Figure 6: **Reference frames used in the camera model. The inertial J2000 ($J2K$), spacecraft (SC), and optics ($OP3$) frames.**

A geometric camera calibration algorithm will then be described, which is used to estimate camera parameters such as focal length, distortion, and alignment. On-orbit results of the camera calibration from a single full-frame image are presented. Finally, flight telemetry is analyzed to show how the star-tracker-to-payload alignment changes over time and how this can be modeled in the frequency domain.

2. Camera Model

The function of the camera model is to take in the spacecraft attitude quaternion as well as the piezo stage position and simulate an image of the star field observed by the payload. This camera model can be used in a high-fidelity, time-domain simulation used to assess the spacecraft performance. In this paper, it is used to analyze the centroiding performance and it is used in the geometric camera calibration procedure. This model is split into a geometric camera model and an imager model and will be described in the following two subsections.

Geometric Camera Model

The geometric camera model uses the spacecraft attitude quaternion to calculate the location of all the star centroids that land on the imager. Fig. 6 shows a picture of the relevant reference frames: the inertial J2000 frame ($J2K$), spacecraft frame (SC), and optics frame ($OP3$).

The first step is to use a star catalog to compute the star unit vectors in the inertial frame,

$$\boldsymbol{v}_{J2K} = \begin{bmatrix} \cos\delta\cos\alpha \\ \cos\delta\sin\alpha \\ \sin\delta \end{bmatrix}, \tag{1}$$

where α is the right ascension and δ is the declination of a given star. ASTERIA uses the Hipparcos star catalog [12], which, in addition to right ascension and declination, provides proper motion information that can be used to propagate the stars from the J1991.25 epoch to the current time. Given additional information about the position and velocity of the camera, the star unit vectors can also be adjusted to account for parallax and stellar aberration.

The stars then need to be transformed to the $OP3$ frame from the $J2K$ frame. The transformation can be computed as

$$\boldsymbol{q}_{OP3\leftarrow J2K} = \boldsymbol{q}_{OP3\leftarrow SC} \otimes \boldsymbol{q}_{SC\leftarrow J2K}, \tag{2}$$

where $\boldsymbol{q}_{SC\leftarrow J2K}$ varies and is the transformation to the SC frame from $J2K$ frame, $\boldsymbol{q}_{OP3\leftarrow SC} = [0.5 \quad 0.5 \quad 0.5 \quad 0.5]^T$ is the nominal transformation to $OP3$ from SC as shown in Fig. 6, and $\otimes$ denotes quaternion multiplication. With this quaternion the inertial star unit vectors can be transformed to the $OP3$ frame,

$$\begin{bmatrix} \boldsymbol{v}_{OP3} \\ 0 \end{bmatrix} = \boldsymbol{q}_{OP3\leftarrow J2K} \otimes \begin{bmatrix} \boldsymbol{v}_{J2K} \\ 0 \end{bmatrix} \otimes \boldsymbol{q}^{-1}_{OP3\leftarrow J2K}, \tag{3}$$

where $\boldsymbol{q}^{-1}$ denotes the quaternion inverse or conjugate. Note that this equation assumes that the fourth element of the quaternion is the scalar.

Since some stars will end up outside the field of view of the optics, it is important to ignore stars that meet the following criteria,

$$\boldsymbol{b}^T_{OP3}\boldsymbol{v}_{OP3} < \cos\frac{FOV}{2}, \tag{4}$$

where $\boldsymbol{b}_{OP3} = [0 \quad 0 \quad 1]^T$ is the camera boresight, which is aligned with the z-axis of the $OP3$ frame for ASTERIA, as shown in Fig. 6, and FOV is the field of view of the optics.

These star unit vectors are now projected onto the two-dimensional image space. The normalized star centroid location in the two-dimensional optics ($OP2$) frame are computed as

$$\begin{bmatrix} u_n \\ v_n \end{bmatrix} = -\frac{1}{z}\begin{bmatrix} x \\ y \end{bmatrix}, \tag{5}$$

where

$$[x \quad y \quad z]^T = \boldsymbol{v}_{OP3}. \tag{6}$$

Note that in eq. (5), the image inversion is explicitly modeled with a negative sign instead of hiding it in the frame definition. Also in this equation, it is again assumed that the z-axis is the optical boresight.

The normalized star centroid locations are then distorted using the radial and tangential distortion model seen in [13]. This model uses the radial and decentering distortions first adapted in [14] and [15]. Examples of how these distortions can change the location of centroids in general can be seen in Fig. 7.

The radial distortions are computed as

$$r_u = (k_1 r_n^2 + k_2 r_n^4 + k_3 r_n^6)u_n \tag{7}$$

and

$$r_v = (k_1 r_n^2 + k_2 r_n^4 + k_3 r_n^6)v_n \tag{8}$$

and the tangential distortions are computed as

$$t_u = 2p_1 u_n v_n + p_2(r_n^2 + 2u_n^2) \tag{9}$$

and

$$t_v = p_1(r_n^2 + 2v_n^2) + 2p_2 u_n v_n, \tag{10}$$

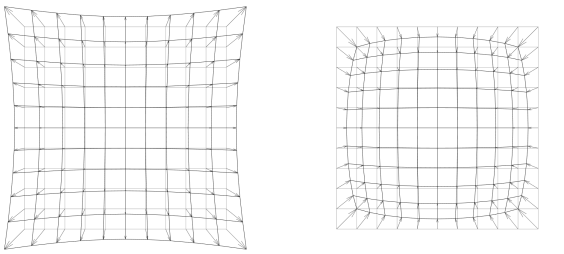

(a) Pincushion distortion, $+k_1$

(b) Barrel distortion, $-k_1$

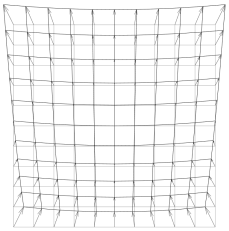

(c) Tangential distortion, $+p_1$

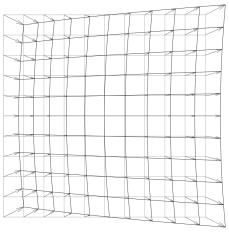

(d) Tangential distortion, $+p_2$

Figure 7: **Examples of radial and tangential distortions.**

where

$$r_n^2 = u_n^2 + v_n^2, \tag{11}$$

$k_1 = 0.4$, $k_2 = -1.7$, and $k_3 = 0$ are the nominal radial distortion parameters, and $p_1 = 0$ and $p_2 = 0$ are the nominal tangential distortion parameters for ASTERIA. The radial distortion parameters were determined by fitting them to a distortion versus field angle plot generated using a model of the optics in Zemax, an optical design and analysis suite. The tangential distortions were assumed to be zero since these are the result of manufacturing tolerances (decentering of lens elements and tilt of the focal plane).

The distorted star centroid positions from the OP2 frame in the $OP2$ frame are computed as

$$\boldsymbol{p}_{OP2}^{c\leftarrow OP2} = f \begin{bmatrix} u_n + r_u + t_u \\ v_n + r_v + t_v \end{bmatrix}, \tag{12}$$

where $f = 85$ mm is the nominal focal length of the camera for ASTERIA.

These star centroids must now be transformed to the imager frame. Since ASTERIA's payload has the imager mounted on a piezo stage platform that translates relative to the lens, this tranformation involves more reference frames than a typical camera. Fig. 8 depicts the various reference frames: the optics frame ($OP2$), piezo stage reference frame (PZR), piezo stage platform frame (PLT), imager frame (IMG), and window frame (WIN).

The star centroids are first converted to the PZR frame, then to the PLT frame, and finally to the IMG frame as

$$\boldsymbol{p}_{PZR}^{c\leftarrow PZR} = \boldsymbol{M}_{PZR\leftarrow OP2}(\boldsymbol{p}_{OP2}^{c\leftarrow OP2} - \boldsymbol{p}_{OP2}^{PZR\leftarrow OP2}), \tag{13}$$

$$\boldsymbol{p}_{PLT}^{c\leftarrow PLT} = \boldsymbol{M}_{PLT\leftarrow PZR}(\boldsymbol{p}_{PZR}^{c\leftarrow PZR} - \boldsymbol{p}_{PZR}^{PLT\leftarrow PZR}), \tag{14}$$

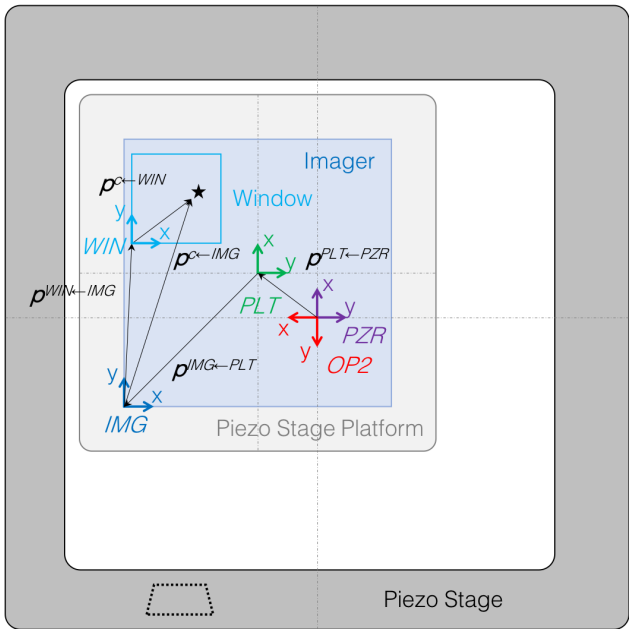

Figure 8: **Reference frames on the focal plane as viewed looking down from the lens. The optics ($OP2$), piezo stage reference (PZR), piezo stage platform (PLT), imager (IMG), and window (WIN) frames. Not to scale.**

and

$$\boldsymbol{p}_{IMG}^{c\leftarrow IMG} = \boldsymbol{M}_{IMG\leftarrow PLT}(\boldsymbol{p}_{PLT}^{c\leftarrow PLT} - \boldsymbol{p}_{PLT}^{IMG\leftarrow PLT}), \tag{15}$$

where $\boldsymbol{p}_{OP2}^{PZR\leftarrow OP2} = [0 \quad 0]^T$ is the position of the PZR frame from the $OP2$ frame in the $OP2$ frame, $\boldsymbol{p}_{PZR}^{PLT\leftarrow PZR}$ varies and is the piezo stage position, $\boldsymbol{p}_{PLT}^{IMG\leftarrow PLT} = [-7.12075 \quad -8.42075]^T$ mm is the nominal imager location on the moving piezo stage platform,

$$\boldsymbol{M}_{PZR\leftarrow OP2} = \begin{bmatrix} 0 & -1 \\ -1 & 0 \end{bmatrix}, \tag{16}$$

$$\boldsymbol{M}_{PLT\leftarrow PZR} = \boldsymbol{I}_{2\times 2}, \tag{17}$$

and

$$\boldsymbol{M}_{IMG\leftarrow PLT} = \begin{bmatrix} 0 & 1 \\ 1 & 0 \end{bmatrix}, \tag{18}$$

by definition, as seen in Fig. 8.

The star centroids are then converted to pixels as

$$\boldsymbol{c}_{IMG} = \frac{\boldsymbol{p}_{IMG}^{c\leftarrow IMG}}{p}, \tag{19}$$

where $p = 6.5$ µm is the pixel pitch of the imager.

Only stars that land on the imager itself are considered,

$$[0 \quad 0]^T \leq \boldsymbol{c}_{IMG} \leq [n_c - 1 \quad n_r - 1]^T, \tag{20}$$

where n_c and n_r are the width and height of the imager in pixels, respectively.

At this point, it is important to note one important implementation issue. The radial and tangential distortions in eqs. (7) through (12) can actually cause stars well outside

the field of view of the camera to "fold over" and appear to land on the imager. This is a modeling issue and does not occur in reality. This occurs because the distortions, r_u, r_v, t_u, and t_v, can grow large for large values of u_n and v_n, which, when added together in eq. (12), can result in small numbers, making a star centroid land on the imager. If selecting the FOV parameter in eq. (4) is not sufficient to throw out these stars, it may be necessary to implement an additional check. One simple method is to compute the centroid locations using a pinhole camera model. This can be done by setting $r_u = r_v = t_u = t_v = 0$ in eq. (12). If the pinhole-model centroids do not land on or near the imager, then the distortion-model centroids should also not land on the imager.

Finally, if desired, the star centroids can be converted to a location on a particular window of the imager as,

$$\boldsymbol{c}_{WIN} = \boldsymbol{c}_{IMG} - \boldsymbol{w}_{IMG}, \tag{21}$$

where $\boldsymbol{w}_{IMG}$ is the position of the window (WIN) frame from the IMG in the IMG frame in pixels, and only stars that land on the window are considered,

$$\begin{bmatrix} 0 & 0 \end{bmatrix}^T \leq \boldsymbol{c}_{WIN} \leq \begin{bmatrix} n_w - 1 & n_w - 1 \end{bmatrix}^T, \tag{22}$$

where $n_w = 64$ pixels is the size of the window.

Imager Model

The imager model then takes the centroid location as an input and generates synthetic windowed star images as they would be produced by the payload in flight. Simulation parameters include a variety of astronomical, optical, and electrical parameters that allow the generation of windows under varying conditions. The simulation begins by precomputing several quantities that are used in later steps. It then forms a windowed image by starting with a modeled point spread function (PSF), scaling the flux according to the assigned star magnitude, binning the flux onto detector pixels, applying physical and electronic noise processes, and converting the flux per pixel to digital values in a manner consistent with the real imager electronics. The complete list of precomputation and image generation steps are listed below and are described in the paragraphs that follow.

Precomputation

1. Generate a theoretical PSF
2. Compute the incident flux from the star being imaged
3. Compute the incident flux due to stray light
4. Generate a dark-current non-uniformity (DCNU) map
5. Generate a photo-response non-uniformity (PRNU) map
6. Generate a subpixel-sensitivity map

Image Generation

1. Place the PSF at the desired subpixel location
2. Multiply the PSF with the subpixel sensitivity map
3. Pixelate and normalize the resultant PSF
4. Compute the stellar flux per pixel
5. Compute the stray light flux per pixel
6. Multiply flux per pixel with the PRNU map
7. Compute dark current per pixel using the DCNU map
8. Compute read noise per pixel
9. Sum flux, dark current, and read noise values
10. Saturate below zero and above the full-well capacity
11. Convert from electrons per pixel to volts
12. Apply the analog-to-digital converter (ADC) gain and offset
13. Saturate volts
14. Convert from volts to counts
15. Add column offsets
16. Quantize and saturate counts

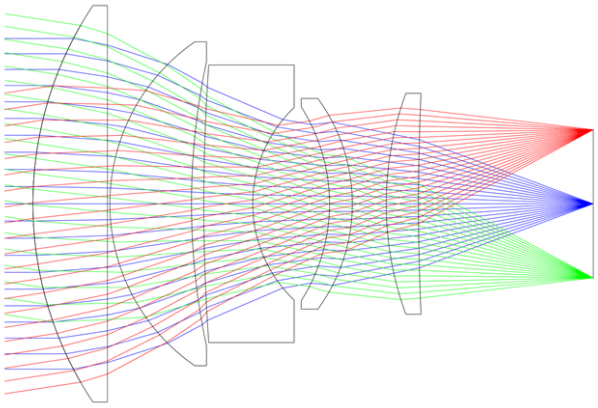

Figure 9: **Telescope lens design using five refractive elements.**

Point Spread Function (PSF) Generation—The ASTERIA optical telescope is a refractive design consisting of five lens elements arranged in a cylindrical aluminum housing. Fig. 9 shows the layout of the lens elements.

A Zemax model of the optics was used to generate a set of predicted PSFs with varying degrees of aberration. A Monte Carlo simulation consisting of 100 trials was run, with each trial applying random amounts of decenter on each of the five lenses. The amount of decenter applied was bounded by the mechanical tolerances of the lenses and housing. For each trial, tilt compensation was added at the image plane—emulating focal plane tilt compensation applied via shims when building the hardware—and PSFs were generated at multiple field points. These PSFs represent the flux distribution at the focal plane when imaging a point source at infinity (i.e. a star). Fig. 10 shows one such PSF. This example is particularly aberrated—much more so than the images from the as-built and as-flown payload—but it was selected to serve as a bounding worst case for analysis to come. Note that the modeled PSF size does not match the window size and must be remapped onto a new grid as a part of the image generation process.

Stellar Flux—The total stellar flux Φ_S arriving at the entrance pupil of the telescope is given by the standard definition of V magnitude,

$$\Phi_S = \Phi_0 \cdot 10^{-V/2.5} \tag{23}$$

where $\Phi_0 = 9.6 \times 10^{10}$ photons/m^2/s/μm is the flux at Vega ($V = 0$) [16]. The signal contained within the PSF at the focal plane S_P is then given by

$$S_P = \Phi_S \cdot \frac{\pi D^2}{4} \cdot \tau \cdot \Delta\lambda \cdot QE \cdot I(\theta) \cdot t \tag{24}$$

where $D = 0.06$ m is the effective aperture diameter, $\tau = 0.8$ is the average transmission over the pass band and field of view, $\Delta\lambda = 400$ nm is the pass band (500 nm to 900 nm), $QE = 0.42\,\mathrm{e}^-$/photon is the average quantum efficiency over the pass band when converting photons to electrons (e^-), $I(\theta)$ is the field-angle-dependent relative illumination on the focal plane, and t is the integration time.

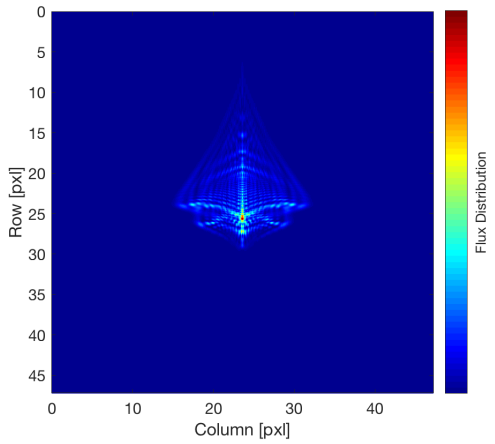

Figure 10: **Example point spread function (PSF).**

Stray Light Flux—The imaging simulation includes a stray light contribution from the Moon. A detailed stray light analysis was not conducted. Instead, the stray light contribution was computed based on reasonable assumptions and the limited test and analysis data that was available. The incident flux from the moon is given by

$$\Phi_M = \Phi_0 \cdot 10^{12.74/2.5} \text{ photons/m}^2\text{/s/µm} \tag{25}$$

where the lunar apparent visual magnitude $V = -12.74$ is from [17]. The general equation for flux at the focal plane due to lunar stray light is,

$$S_M = \Phi_M \cdot \cos\theta_M \cdot \frac{\pi D_B^2}{4} \cdot \rho^n \cdot \tau \cdot \Delta\lambda \cdot QE \cdot t \cdot \frac{1}{n_r n_c} \tag{26}$$

where θ_M is the moon off-axis angle from the payload boresight, $D_B = 0.01$ m is the diameter of the baffle, $\rho = 0.045$ is the baffle reflectivity, n is the number of reflections from first hitting the baffle until reaching the focal plane, n_r is the number of rows in the imager and n_c is the number of columns in the imager.

As a simplifying assumption, this equation models the stray light flux as being uniformly distributed over the focal plane. The units of S_M are therefore electrons per pixel. Numerical analysis of the ASTERIA baffle and lens assembly showed that for angles of 45 degrees or greater, incident rays will undergo at least two reflections from surfaces that had been painted black, therefore $\theta_M = 45°$ and $n = 2$.

Dark-Current Non-Uniformity (DCNU) Map—The next step is creating a map of dark current over the simulated window. This involves (1) determining the DCNU map at a reference temperature and (2) generating dark current values for each pixel at the operating temperature. DCNU is the variation in dark current from pixel to pixel. Based on measurements of the Fairchild detector (see Fig. 24 and surrounding discussion), it was determined that the dark current value in each pixel follows a log-normal distribution. The dark current value of a pixel is given by

$$S_{D_0} = \exp(\mu + \sigma Z), \tag{27}$$

where

$$\mu = \ln\left(\frac{m_{D_0}}{\sqrt{1 + \frac{s_{D_0}^2}{m_{D_0}^2}}}\right), \tag{28}$$

$$\sigma = \sqrt{\ln\left(1 + \frac{s_{D_0}^2}{m_{D_0}^2}\right)}, \tag{29}$$

$m_{D_0} = 40.1$ e$^-$/pixel/s is the mean dark current, $s_{D_0} = 28.6$ e$^-$/pixel/s is the dark-current non-uniformity, both measured at a reference temperature of $T_0 = 305$ K, and $Z \sim \mathcal{N}(0,1)$ is a standard normal random variable. The DCNU map for reference temperature T_0 is created by drawing samples from this log-normal distribution for each pixel in the window.

Next the S_{D_0} values are used to calculate the dark current at each pixel for an arbitrary detector temperature. The mean dark current signal in each pixel S_D due to thermal processes within the detector is given by [18, eq. 7.43]

$$S_D = CT^{1.5} \exp\left(\frac{-E_g}{2kT}\right) \tag{30}$$

where C is a constant, $T = 303$ K is the detector operating temperature, E_g is the silicon bandgap energy, and $k = 8.62 \times 10^{-5}$ eV/K is Bolzmann's constant. The bandgap energy E_g varies with temperature following an empirical formula given by [18, eq. 7.44],

$$E_g = 1.1557 - \frac{7.021 \times 10^{-4} T^2}{1108 + T} \tag{31}$$

We can solve eq. (30) for C by measuring the dark current signal S_{D_0} at a reference temperature T_0,

$$C = \frac{S_{D_0}}{T_0^{1.5} e^{-E_{g_0}/(2kT_0)}} \tag{32}$$

where E_{g_0} is the bandgap energy calculated for T_0 using eq. (31).

Inserting the random samples S_{D_0} into eq. (32) and calculating a new set of dark current values S_D using eq. (30), a map of dark current over a window at temperature T is obtained, as shown in Fig. 11. Multiplying the dark current values by the integration time t yields a dark current signal in electrons per pixel.

Photo-Response Non-Uniformity (PRNU) Map—The variation in sensitivity from pixel to pixel or PRNU was incorporated into the model by drawing random pixel sensitivity values from a normal distribution with $\mu = 1$ and $\sigma = 0.03$, corresponding to the datasheet PRNU value of 3%. Fig. 12 shows the resulting PRNU map.

Subpixel Sensitivity Map—In addition to PRNU effects between pixels, silicon-based array detectors exhibit variations in sensitivity within individual pixels. These subpixel or "intrapixel" sensitivity variations have been measured in both CCDs [19] and CMOS devices [20]. Due to schedule constraints, the subpixel sensitivity of the Fairchild CIS2521F0111 imager was not measured. Instead a Gaussian subpixel sensitivity function was applied,

$$s(x,y) = \exp\left(-\frac{(x-x_0)^2 + (y-y_0)^2)}{2\sigma^2}\right) \tag{33}$$

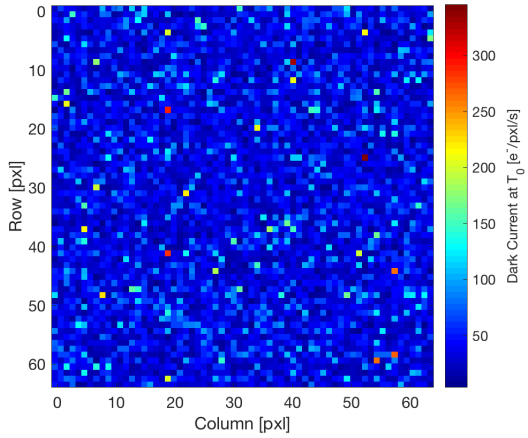

Figure 11: **Dark-current non-uniformity map.**

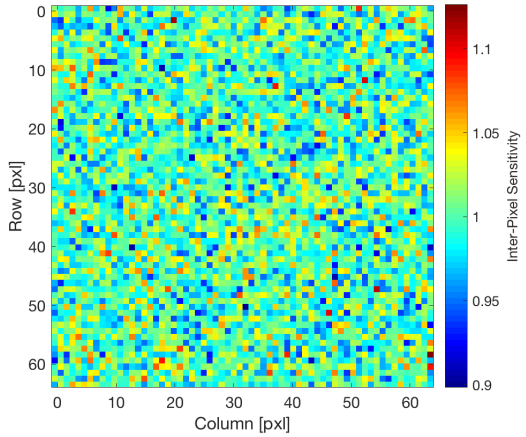

Figure 12: **Photo-response non-uniformity map.**

where s is relative sensitivity, (x, y) defines a local coordinate system centered on the pixel, (x_0, y_0) are the in-plane offsets of the subpixel response surface with respect to the pixel center, and σ_{sp} parameterizes the width of the Gaussian. The results contained here use $x_0 = 0.1$ pixel, $y_0 = 0.2$ pixel, and $\sigma = 0.3$ pixel. Fig. 13 shows the subpixel sensitivity map for a single pixel. This map is replicated over all pixels in a window, as shown in Fig. 14.

Image Generation— Having performed the computations above, generating the simulated image begins with placing the PSF at the desired subpixel location on the window grid, which can be done via two-dimensional interpolation. The PSF is then multiplied by the subpixel sensitivity map, resulting in Fig. 15.

The next step is to pixelate the image by down-sampling the fine grid—used to define the detailed PSF structure and sub-pixel contours—into pixel-sized bins. The resulting pixelated PSF is also normalized such that the sum of all values in the window is unity. This is done in preparation for adding stellar flux levels in the next step. Fig. 16 shows the pixelated PSF.

With the pixelated, normalized PSF in hand, the next step is to simply multiply each pixel by the value given by the stellar flux level, S_P, given in eq. (24). Because S_P represents the

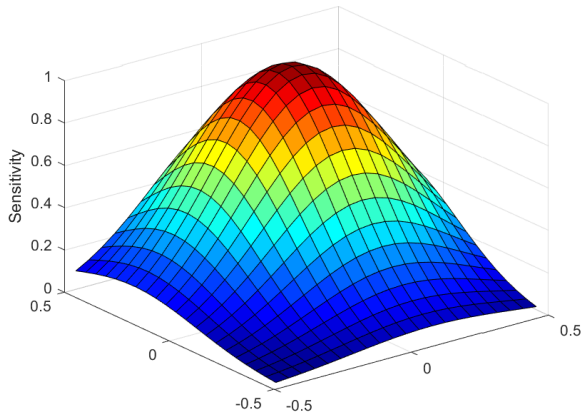

Figure 13: **Subpixel sensitivity map for a single pixel.**

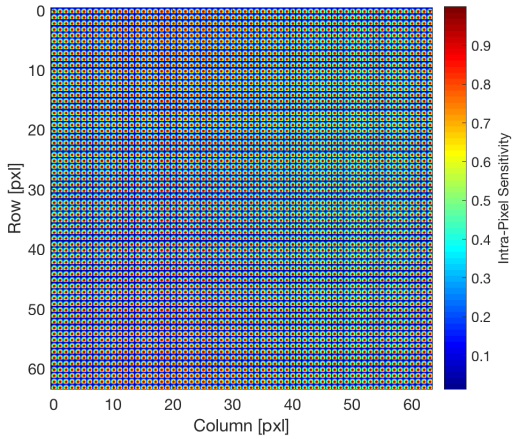

Figure 14: **Subpixel sensitivity map, achieved by replicating the single-pixel sensitivity map to all pixels in the window.**

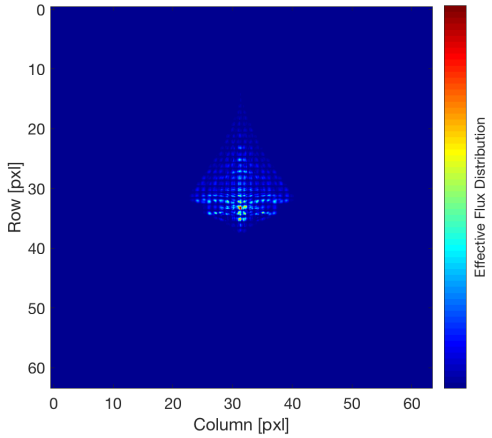

Figure 15: **Subpixel point spread function.**

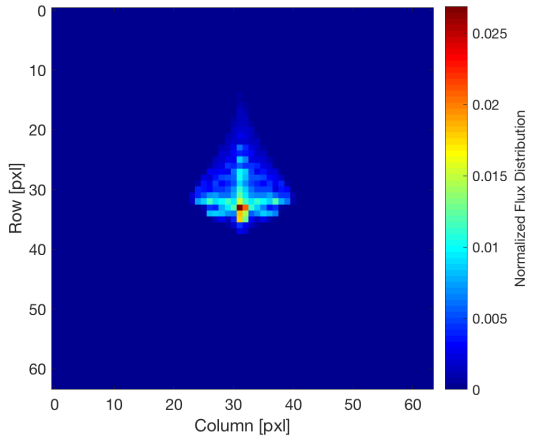

Figure 16: **Pixelated point spread function.**

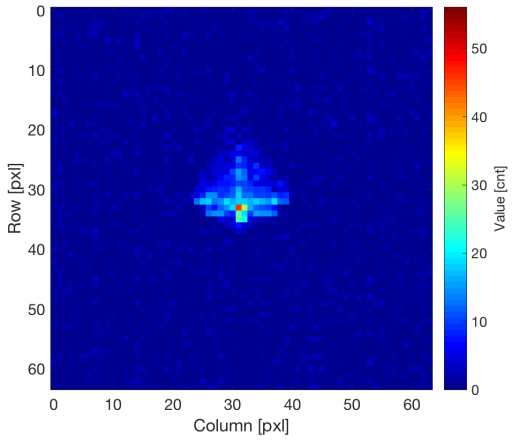

Figure 17: **Simulated windowed image before adding column offsets.**

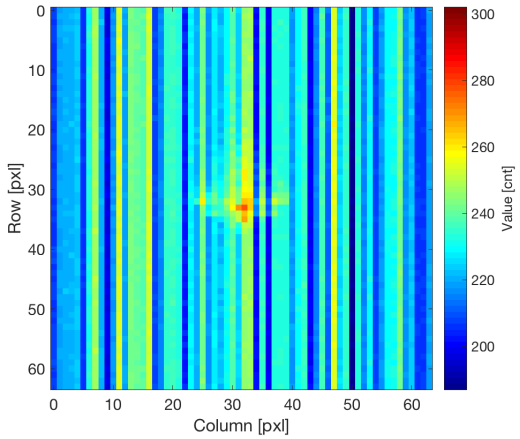

Figure 18: **Final simulated windowed image.**

total amount of stellar flux contained in the PSF, multiplying by a pixelated PSF that has been normalized to unity will give the correct distribution of mean electrons per pixel. To properly account for photon shot noise, pixel values for the stellar signal are drawn from a Poisson distribution that uses the mean electrons per pixel as the distribution parameter.

The stray light signal is computed in a similar manner as the stellar signal. The stray light signal per pixel, S_M, is given by eq. (26) and to account for shot noise, S_M is used as the parameter when drawing samples from a Poisson distribution. Both of these arrays—stellar signal and stray light signal—are each multiplied by the PRNU map to account for pixel-to-pixel sensitivity variations.

The next step is computing an array that represents the dark current signal per pixel. This is accomplished by using the mean dark current signal per pixel (i.e. DCNU map S_D in Fig. 11 multiplied by integration time t) as the parameter in a Poisson distribution to add shot noise effects.

The final contribution to the array of raw pixel values is read noise, which is simulated by drawing values from a normal distribution with zero mean and $\sigma = 5.7$ e^-/pixel as measured in the laboratory (see Fig. 23 and surrounding discussion).

The stellar flux array, stray light flux array, dark current array, and read noise array are summed to compute the total charge per pixel S_{e^-}. Values larger than the full well capacity are set to the datasheet value of 30,000 e^- and negative values are set to zero.

The signal can now be converted from e^- to counts as

$$S_{\mathrm{cnt}} = \frac{2^{n_b} - 1}{\Delta v} \cdot g_{\mathrm{PGA}} \cdot g_{V/\mathrm{e}^-} \cdot S_{\mathrm{e}^-}, \tag{34}$$

where $g_{V/\mathrm{e}^-} = 40$ μV/e^- is the conversion gain based on values from the datasheet, $g_{\mathrm{PGA}} = 1.94$ is the as-measured analog gain of the programmable gain amplifier (see Fig. 22 and surrounding discussion), $\Delta v = 1.021$ V is the voltage range of the analog-to-digital converter (ADC), and $n_b = 11$ is the number of bits in the ADC. An example of the post-ADC image is shown in Fig. 17.

The Fairchild CIS2521F has a set of fixed offsets that are added to each column during read-out, which is included in the simulation. See Fig. 21 and the surrounding discussion. The column offsets are likely due to differences in offsets between the column amplifiers.

After applying the column offsets, the last step is to quantize the pixel counts by flooring the values to integers, setting any negative values to zero, and saturating values at a maximum of $2^{n_b} - 1$. An example of the final simulated window is shown in Fig. 18.

Laboratory Measurements of Imager Parameters

Simple measurements were taken in the laboratory to obtain some of the key imager parameters. Note that some of these methods of taking data could have been improved and some tests were omitted given the very tight time constraints between having a functioning flight payload and delivery of the spacecraft.

Before discussing the measurements that were taken, it is important to understand the layout of the pixels in the imager, which is shown in Fig. 19. This shows that the imager has a 16-pixel border of optically and electrically dark pixels. The optically and electrically dark pixels are covered with metal,

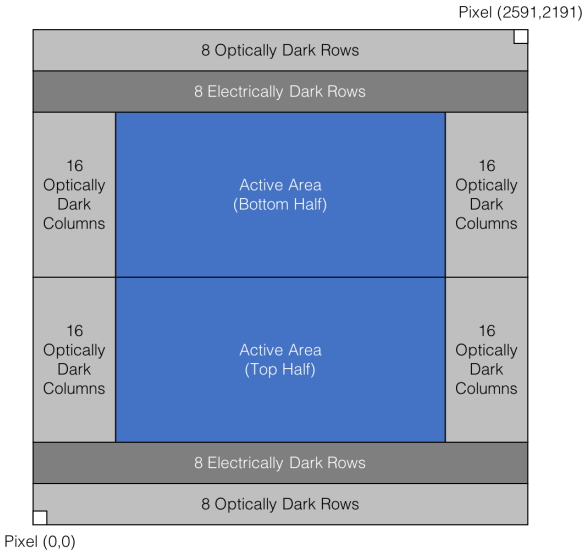

Figure 19: **Fairchild CIS2521F pixel layout as viewed looking down from the lens. Not to scale.**

ensuring that light cannot illuminate these pixels. In addition, the electrically dark pixels are tied to ground, removing any dark current that is built up on these pixels. Also, note that the imager is split into a top half and bottom half. The imager can be thought of as two separate imagers placed side by side and the following analyses will compute values for the top and bottom half separately to see if there is a difference in performance between the two.

The column offsets were computed by taking many full-frame images at the high-gain setting. An example full-frame image is shown in Fig. 20. This clearly shows that the columns do indeed have an offset and the offset is different for the top and bottom halves of the imager. The mode of the electrically dark rows were taken across frames and rows for the top and bottom halves of the imager. A histogram of these offsets are shown in Fig. 21. These offsets are necessary to be able to upload as parameters for the on-board centroiding algorithm that will be discussed in Section 3. Note that it was later determined that the column offsets change slightly when operating the imager in the full-frame versus windowed mode. Since the centroiding is always performed in the windowed mode, the column offsets should have been gathered in the windowed mode during ground testing.

The imager analog voltage gain was determined by taking many full-frame images of a flat field at both the low-gain and high-gain settings and correcting the column offsets. The active area of the low-gain and high-gain images were averaged separately, then the high-gain image was divided, pixel-by-pixel, by the low-gain image to obtain the gain for each pixel. A histogram of the gain values are shown in Fig. 22 and show an average gain of 1.94, which is close to the expected value of 2.

The read noise was calculated by analyzing the electrically dark pixels after the column correction. These pixels should not accumulate charge from photons or dark current and their values should therefore be influenced only by read noise. The standard deviation of each of the electrically dark pixels were computed over many frames and the histogram of these standard deviations are shown in Fig. 23. This shows a read

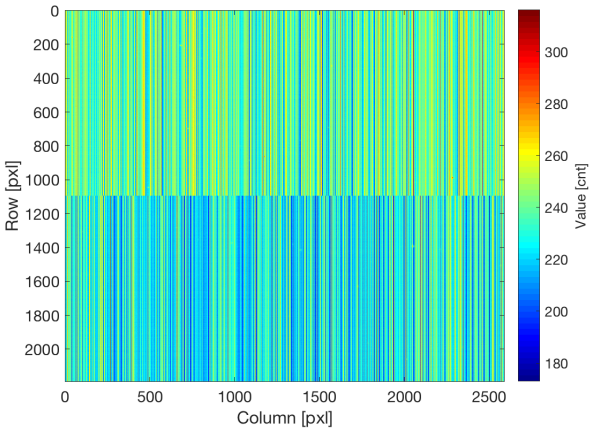

Figure 20: **Example raw full-frame image showing different column offsets for the top and bottom halves of the imager.**

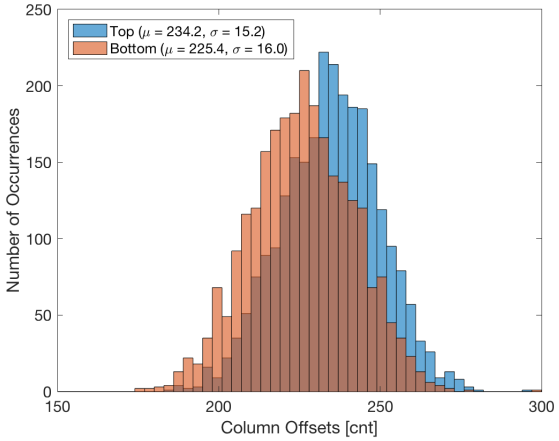

Figure 21: **Histogram of the column offsets present in the top and bottom halves of the imager.**

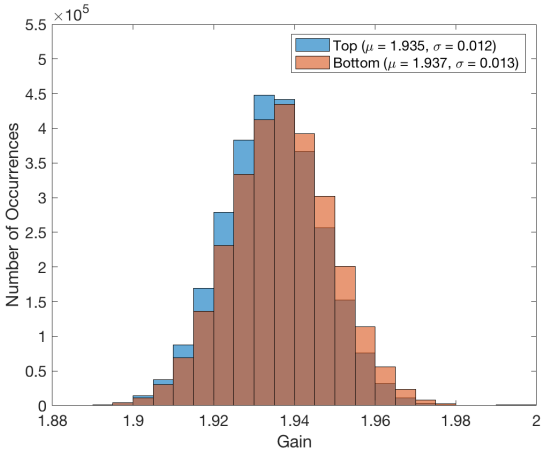

Figure 22: **Histogram of the analog voltage gain of each active pixel.**

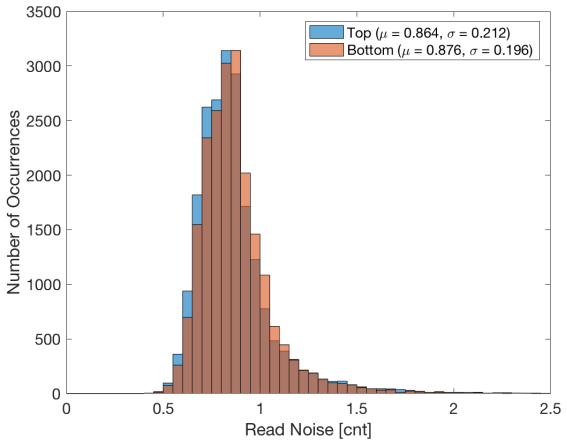

Figure 23: **Histogram of read noise for each electrically dark pixel.**

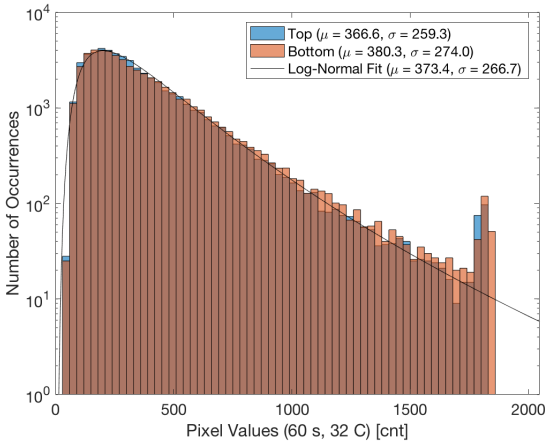

Figure 24: **Histogram of optically dark pixel values for an integration time of 60 s at 32 C.**

noise of 5.7 e^-, with a conversion gain of 0.155 cnt/e^-. This is higher than expected since the datasheet reported a read noise of 2 e^- when using a 30x gain setting. In hindsight, the read noise is likely lower for higher gain setting and it might have been advantageous to use a higher gain setting. This would have to have been specified when the imager electronics board was being designed since using the higher gain settings requires different pin connections.

The dark-current non-uniformity was determined by taking many long-duration full-frame images. The optically dark pixels were column-corrected and averaged over the frames. An integration time of 60 s provided a good balance between building up charge on many pixels and avoiding saturation. The histogram of these pixel values are shown in Fig. 24. There is little difference between the top and bottom and the histogram matches very well to a log-normal distribution. The bump at the high-end of pixel values are due to a small number of pixels saturating and the column-offset correction bringing those values down away from saturation. This plot shows a average dark durrent of 40.1 e^-/pxl/s and dark-current non-uniformity or standard deviation of 28.6 e^-/pxl/s, with a conversion gain of 0.155 cnt/e^-, integration time of 60 s, and temperature of 32 C. These numbers are on the same order of magnitude as the datasheet, which quotes a dark current of 35 e^-/pxl/s and dark-current non-uniformity of 65 e^-/pxl/s at 20 C.

The optically and electrically dark pixels on the imager enabled the measurement of various imager parameters with very simple tests involving taking full-frame images. These parameters were used to update the imager model before flight.

Simulated vs. Measured Images

Figs. 25 and 26 show actual raw and corrected images of the star HD 219134, respectively. This can be directly compared against Figs. 18 and 17, which are simulations of a star with the same V magnitude. The column offsets are a bit different between the simulated and measured raw images since the simulated column offsets are from a full-frame image while a windowed image has slighly different column offsets. In the corrected images, the noise and signal levels in the simulated and measured images qualitatively match. The PSF shape is clearly different because no attempt was made

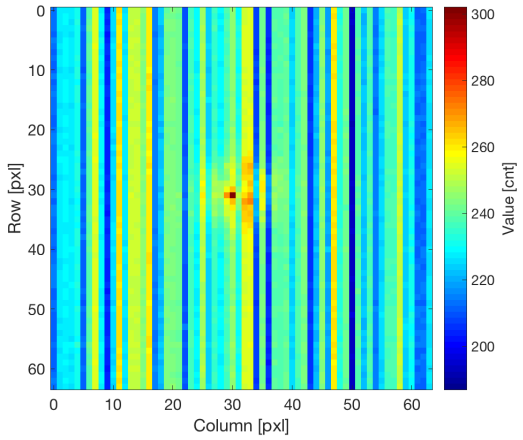

Figure 25: **Measured, raw, windowed image of HD 219134.**

to model the on-orbit PSFs to incorporate into the simulation. Nevertheless, this does provide a high-level validation of the imager model.

3. CENTROIDING

This section will discuss the on-board centroiding algorithm, some results of the centroiding algorithm run on simulated images, and compare those results against on-orbit centroiding telemetry.

Centroiding Algorithm

The centroiding algorithm that will be presented is the flight algorithm and it assumes that the input will be a windowed image of a single star. It is based on algorithms that can be found in literature such as the one in [21], but contains modifications to correct for column offsets and reject temporarily bright or hot pixels.

The first step is to compute the average value of background pixels. It does this by computing the average value of the top

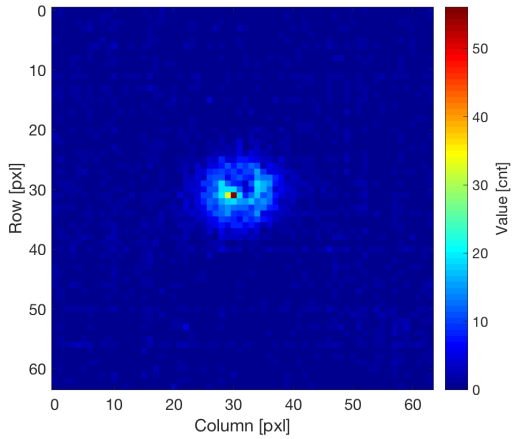

Figure 26: **Measured, corrected, windowed image of HD 219134.**

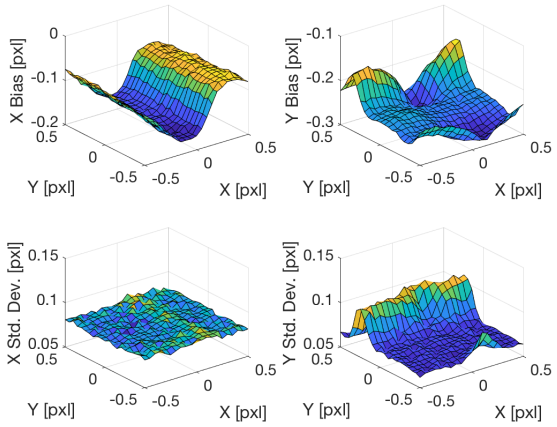

Figure 27: **Centroiding bias and standard deviation over a pixel for a simuated V magnitude 6 star.**

and bottom rows of the window as

$$b = \frac{\sum_{j=0}^{n-1} \left[\max(p_{0,j} - o_j, 0) + \max(p_{n-1,j} - o_j, 0)\right]}{2n}, \tag{35}$$

where $p_{i,j}$ is the raw pixel value of the zero-indexed i^{th} row and j^{th} column of the windowed image, o_j is the offset for column j, $n = 64$ pixels is the size of the window, and the $\max$ function ensures that the column-offset subtraction does not bring the corrected pixel value below zero. The left and right columns were left out for simplicity but can be included in this calculation, if desired. Note that this assumes that there are no stars or otherwise bright pixels in the border. This is ensured to be the case by selecting guide stars with no nearby, bright neighbors.

The next step is to search the window for the approximate star centroid location. Simply searching for the brightest pixel in the window can result in making the algorithm sensitive to temporarily bright pixels or hot pixels, as seen in [11]. Therefore, the search process will look at the column-corrected, background-subtracted pixel value, $\max(p_{i,j} - o_j - b, 0)$, and if it is greater than a set threshold, the pixel is valid. The brightest pixel can now be searched for by only considering a pixel if it is valid and at least one orthogonally adjacent pixel is also valid. This greatly reduces the probability that the centroiding algorithm will be significantly affected by a temporarily bright pixel or hot pixel.

The centroiding region of interest (ROI) can now be centered on this approximate star centroid location and the center of mass can be computed as

$$\boldsymbol{c}_{WIN} = \frac{\begin{bmatrix} \sum_{i=i_0}^{i_0+m-1} \sum_{j=j_0}^{j_0+m-1} j \max(p_{i,j} - o_j - b, 0) \\ \sum_{i=i_0}^{i_0+m-1} \sum_{j=j_0}^{j_0+m-1} i \max(p_{i,j} - o_j - b, 0) \end{bmatrix}}{\sum_{i=i_0}^{i_0+m-1} \sum_{j=j_0}^{j_0+m-1} \max(p_{i,j} - o_j - b, 0)}, \tag{36}$$

where i_0 and j_0 define the corner of the ROI, and m is the size of the ROI.

The centroid is then converted from the *WIN* frame to the *IMG* frame as

$$\boldsymbol{c}_{IMG} = \boldsymbol{c}_{WIN} + \boldsymbol{w}_{IMG}, \tag{37}$$

where $\boldsymbol{w}_{IMG}$ is the position of the window (*WIN*) frame from the *IMG* in the *IMG* frame in pixels.

Example Centroiding Error

The centroiding algorithm can now be run on a set of simulated images generated using the imager model presented in Section 2 to predict centroiding errors.

A series of images were created with the star at locations over a grid the size of a pixel. This allows the centroid error to be computed as a function of centroid location on a pixel. Fig. 27 shows the resulting centroid errors, split into a bias and standard deviation for the x and y-directions, for a V = 6 magnitude star.

The biases show a clear "s-curve" error, which repeats with a period of one pixel. The exact shape of these curves are determined mostly by the PSF shape, which, for this simulation, is shown in Fig. 10. The standard deviation is mostly the same value over a pixel except for an increase in the y-direction over a strip of the pixel. These increases in standard deviation tend to appear where there are large gradients in the centroid bias.

Simulated vs. On-Orbit Performance

For ASTERIA, the standard deviation of the centroid error is much more important than the bias. Monte Carlo simulations were run to predict the centroid standard deviation versus V magnitude, which can be used to predict pointing performance for a given star field. These were then compared against on-orbit telemetry to determine how well the model predicted on-orbit performance.

Telemetry from on-orbit observations contain the centroid locations computed at 20 Hz, which can be used to compute the measured, on-orbit centroid standard deviation of the observed guide stars. These centroids, however, contain the actual motion of the centroids over the observation, unlike the simulated centroids, which were held in place. To isolate the actual low-frequency motion from the white centroid noise, the one-sided power spectral density (PSD) and the cumulative mean square value (MSV), integrated from infinity to zero, were computed. These plots for one centroid over multiple observations of the same star field are shown in Fig. 28. This shows that at frequencies below 2

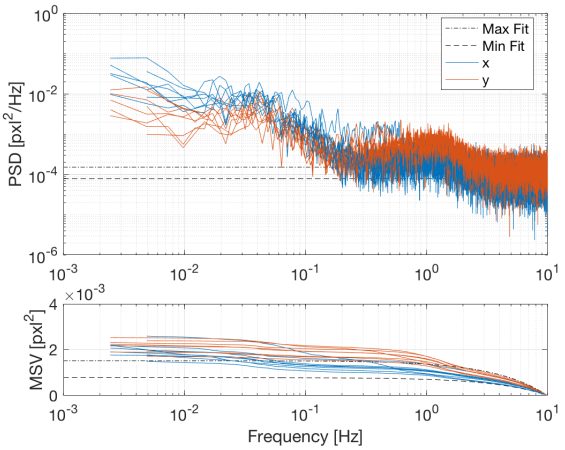

Figure 28: **Power spectral density and cumulative mean square value of centroid movement.**

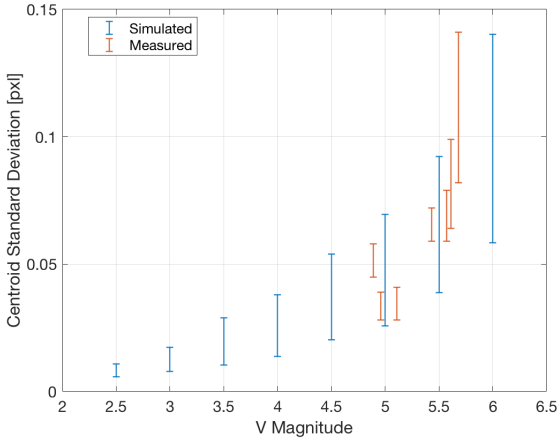

Figure 29: **Simulated versus measured centroid standard deviation versus V magnitude for integration times of 50 ms.**

Hz, the approximate pointing controller bandwidth, the PSD grows—this is the actual centroid motion. For frequencies above 2 Hz, the centroid error flattens out to a noise floor—this is the white centroid noise. A simple one-sided, band-limited, white-noise PSD can be fit to the cumulative MSV for frequencies higher than 2 Hz. This PSD is given by,

$$P(f) = 2\sigma^2 \Delta t, \tag{38}$$

where σ is the centroid standard deviation, $\Delta t = 50$ ms is the sampling period, and f is frequency in Hz. Note that when this PSD is integrated from 0 Hz up to the Nyquist frequency of $1/(2\Delta t)$, the MSV is σ^2, as expected. A minimum value and maximum value centroid standard deviation fit are shown in Fig. 28. It is expected that the measured MSV drifts outside of this range for frequencies below 2 Hz.

The maximum and minimum centroid standard deviations versus V magnitude for the simulation and on-orbit measurements are shown in Fig. 29. For the simulation, a V magnitude range of 2.5 to 6 was chosen as a range that would not saturate the imager on the bright side and not result in a poor signal-to-noise ratio on the dim side. For the measurements, seven guide stars were used for observations of the star field around HD 219134 and their catalog V magnitudes happened to lie within the range of 4.5 to 6. The measured centroid standard devations line up well with the predicted centroid standard deviations, validating the ability to use the imager model to predict centroiding performance at a high level.

4. Geometric Camera Calibration

The goal of geometric camera calibration, or camera resectioning, is to estimate the parameters of a camera model such as focal length, distortion, and alignment. With this model, the location of stars on the focal plane can be predicted for a given spacecraft attitude. This is essential for ASTERIA since the window locations for each guide star must be specified prior to any observation.

The problem of geometric camera calibration has been well researched and there exist common methods for performing this calibration [22, 23]. These methods typically involve taking pictures of a calibration target at multiple distances and orientations and batch processing these images to estimate the camera parameters. However, there are many problems with this approach when applying it to ASTERIA. First, ASTERIA's payload is focused at infinity to image stars, so any images of close-range calibration targets will be blurry. This, combined with the 10-degree field of view of the camera, means that the calibration target would need to be relatively far away and large, making this approach less feasible. In addition, it is unclear how this approach would translate to imaging stars, which are point sources, since the calibration target is typically a grid of circles or squares of finite size. Finally, any geometric camera calibration that is performed on the ground may need to be performed again on orbit anyway due to the differences in temperature and pressure. Therefore, it makes the most sense to do this calibration on orbit by imaging an actual star field. The idea of using a star field to perform geometric camera calibration is not new [14, 24, 25]. However, the problem setup, model parameters, and procedure needed to be modified for use on ASTERIA.

Calibration Procedure

The proposed geometric camera calibration procedure only requires the centroids of a star field image, and the spacecraft attitude and piezo stage position at the time the image was taken. This process can easily be extended to process multiple images. The general idea is to perform a nonlinear least-squares minimization of a cost function,

$$\min_{\boldsymbol{x}} \sum_i (\boldsymbol{c}_{IMG}^{p_i} - \boldsymbol{c}_{IMG}^{m_i})^T (\boldsymbol{c}_{IMG}^{p_i} - \boldsymbol{c}_{IMG}^{m_i}), \tag{39}$$

where $\boldsymbol{c}_{IMG}^{p_i}$ is the i^{th} predicted centroid in pixels, $\boldsymbol{c}_{IMG}^{m_i}$ is the i^{th} measured centroid in pixels, and

$$\boldsymbol{x} = [\delta\phi \quad \delta\theta \quad \delta\psi \quad k_1 \quad k_2 \quad k_3 \quad p_1 \quad p_2 \quad f]^T \tag{40}$$

contains the camera parameters to be optimized. The variables $\delta\phi$, $\delta\theta$, and $\delta\psi$ are roll, pitch, and yaw perturbations in the camera alignment, which are used to construct a delta quaternion,

$$\delta\boldsymbol{q} = \begin{bmatrix} \sin\frac{\phi}{2}\cos\frac{\theta}{2}\cos\frac{\psi}{2} - \cos\frac{\phi}{2}\sin\frac{\theta}{2}\sin\frac{\psi}{2} \\ \cos\frac{\phi}{2}\sin\frac{\theta}{2}\cos\frac{\psi}{2} + \sin\frac{\phi}{2}\cos\frac{\theta}{2}\sin\frac{\psi}{2} \\ \cos\frac{\phi}{2}\cos\frac{\theta}{2}\sin\frac{\psi}{2} - \sin\frac{\phi}{2}\sin\frac{\theta}{2}\cos\frac{\psi}{2} \\ \cos\frac{\phi}{2}\cos\frac{\theta}{2}\cos\frac{\psi}{2} + \sin\frac{\phi}{2}\sin\frac{\theta}{2}\sin\frac{\psi}{2} \end{bmatrix}. \tag{41}$$

This equation assumes that the fourth element in the quaternion is the scalar. Note that even though the roll, pitch, and yaw adjustments will likely end up being small, it is important to not use a small-angle approximation to create the delta quaternion since the optimization algorithm may evaluate the solution with large angles. This delta quaternion is used to adjust the alignment quaternion,

$$\bar{\boldsymbol{q}}_{OP3\leftarrow SC} = \delta\boldsymbol{q} \otimes \boldsymbol{q}_{OP3\leftarrow SC}. \tag{42}$$

One notable distinction between this method and other methods laid out in the literature is that the principal point is not estimated. This is because it was determined that the pitch and yaw elements in the alignment quaternion result in a shift of centroid locations that is indistinguishable from a change in principal point. Therefore, the principal point is left out of the optimization and its nominal value is held constant.

To construct the cost function, the predicted and measured centroids must first be computed. To compute the predicted centroids, the inputs, $\boldsymbol{q}_{SC\leftarrow J2K}$ and $\boldsymbol{p}_{PZR}^{PLT\leftarrow PZR}$, are fed into the geometric camera model presented in Section 2. To compute the measured centroids, the full-frame image can be fed into an algorithm such as the one presented in Section 3, with a few modifications for it to work using a full-frame versus a windowed image.

These measured stars must now be matched to the predicted stars. This can be accomplished through any star identification algorithm such as Pyramid [26]. Instead, for this application, a simple and naïve approach of matching each measured centroid with its nearest predicted centroid was sufficient, though it did require some human intervention to intelligently select the initial parameters. For autonomous calibration applications, a more robust matching algorithm should be used.

Now that the cost function can be evaluated, it can be optimized using a nonlinear optimization algorithm. In MATLAB, a numerical computing environment, the `fminunc` function using the quasi-newton algorithm sufficed.

On-Orbit Calibration Results

A full-frame image of the star field around HD 219134 was captured to perform an on-orbit geometric camera calibration, as shown in Fig. 30. At the time the picture was taken, the attitude was

$$\boldsymbol{q}_{SC\leftarrow J2K} = \begin{bmatrix} +0.8680963044 \\ -0.0952830051 \\ +0.4849758134 \\ +0.0461347548 \end{bmatrix} \tag{43}$$

and the piezo stage position was

$$\boldsymbol{p}_{PZR}^{PLT\leftarrow PZR} = [50 \quad 50]^T \ \mu\text{m}. \tag{44}$$

Fig. 31 shows the predicted and measured centroids using the nominal camera parameter values before the calibration. There is a significant offset between the predicted and measured centroids of approximately 120 pixels, which means that the stars would not have landed in their specified windows since the windows are only 64×64 pixels in size.

For illustrative purposes, the optimization was run with the option of only varying the alignment quaternion, $\bar{\boldsymbol{q}}_{OP3\leftarrow SC}$. Fig. 32 shows the results with magnified residuals between

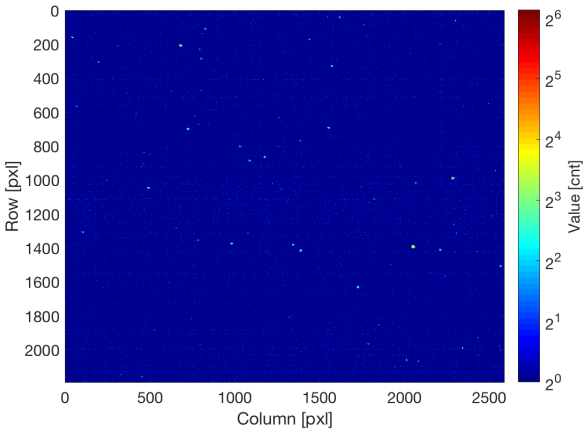

Figure 30: **Full-frame image used for geometric camera calibration.**

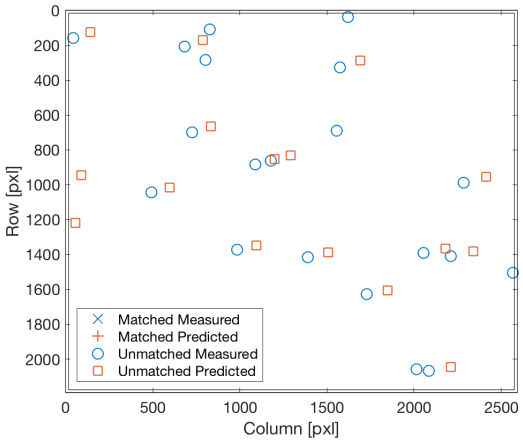

Figure 31: **Predicted and measured centroids before calibration.**

the measured and predicted centroids. The residuals show a clear radial error pattern. Also, note that the number of measured and predicted stars are different due to the centroiding and star catalog thresholds that were selected, and unmodeled variations in stellar spectra.

Fig. 33 shows predicted and measured centroids with the final calibration. The measured and predicted centroid match well, with residual errors showing a standard deviation of 0.5 pixel and no obvious pattern.

Table 1 compares the nominal parameters with the calibrated parameters. Note that the radial and tangential distortion coefficients have remained the same. This was purposefully enforced to be true since allowing those variables to be optimized did not significantly improve the calibration. Also, it turns out the radial errors shown in Fig. 32 are not due to radial distortion, which is a second-order or higher effect (see eqs. (7) and (8)), but rather a roughly 1-mm error in the focal length, which is a first-order effect.

The residual error in the calibration is most likely due to measured centroid biases, which are dependent upon each star's PSF shape, field position, and brightness. Other errors

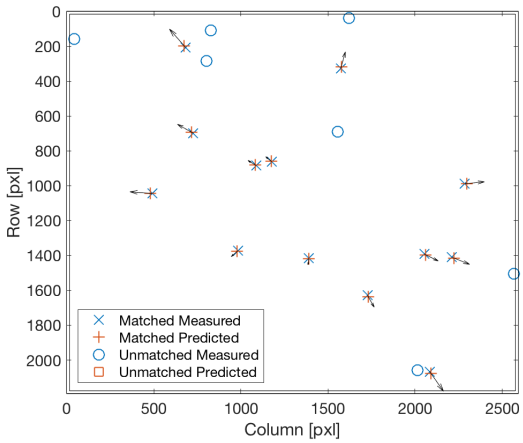

Figure 32: **Predicted and measured centroids with alignment calibration only.**

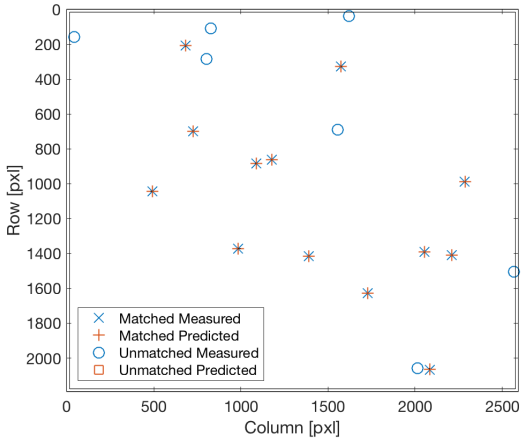

Figure 33: **Predicted and measured centroids after calibration.**

Table 1: **Nominal and calibrated camera parameters**

Parameter	Variable	Nominal	Calibrated
Roll pert.	$\delta\phi$	0 deg	+0.1267 deg
Pitch pert.	$\delta\theta$	0 deg	+0.5023 deg
Yaw pert.	$\delta\psi$	0 deg	-0.1627 deg
Radial coeff. 1	k_1	0.4	0.4
Radial coeff. 2	k_2	-1.7	-1.7
Radial coeff. 3	k_3	0	0
Tan. coeff. 1	p_1	0	0
Tan. coeff. 2	p_2	0	0
Focal length	f	85 mm	83.94 mm

such as star catalog errors, proper motion, parallax, and stellar aberration will have a much smaller effect on the calibration errors. The Hipparcos catalog has errors in right ascension and declination of less than 300 mas [12], which is a very small fraction of a pixel. Proper motion has been accounted for by propagating the star catalog to the current time and errors on those propagated values can be on the order of hundreds of mas [12], which again is insignificant. Parallax can introduce an error on a per-star basis of up to 0.8 arcsec [12], based on the distance to the closest star, Proxima Centauri. This is still a fraction of a pixel and can be ignored. Stellar aberration can produce a common-mode bias in all centroids of up to 20.5 arcsec due to the velocity of Earth around the Sun and 5.3 arcseconds due to the velocity of the spacecraft around Earth at an altitude of 400 km. This can result in a worst-case centroid shift of up to approximately 3 pixels, which is still very small compared to the 64×64 window size. Also, since every star in the field of view is shifted by approximately the same amount on the focal plane, this is indistinguishable with a change in the alignment quaternion.

This calibration procedure and results using a single image has proved to be more than sufficient to predict the location of stars to be able to place them in a 64×64 window for many science observations. This calibration has only needed to be performed once on orbit.

Changes in Camera Calibration Parameters

To get a sense of how much the camera calibration parameters change over the course of an observation, the calibration procedure was run using pointing control telemetry at each 20 Hz time step over an observation. Fig. 34 shows the results. It can be seen that the focal length does change by up to 0.03 mm versus the calibrated focal length shown in Table 1, but this results in errors of a fraction of pixel. On the other hand, the alignment does change by tens of arcseconds, or multiple pixels. It is important to note again that this alignment change is isomorphic to changes in principal point and stellar aberration changes over the course of the observation. These three effects produce the same resulting effect on the payload, but this analysis pins it all on changes in alignment. It is also worth noting that this change in alignment is on the right order of magnitude given the approximate size of the spacecraft, coefficient of thermal expansion of the materials, and thermal gradients that the spacecraft experiences over an orbit.

As a useful input to the overall pointing error budget of ASTERIA as well as a potentially useful data point for other missions, a frequency-domain model of this change in alignment can be developed. The PSD and cumulative MSV of the alignment changes over an observation were computed for many observations. The results are shown in Fig. 35.

A shaping filter can now be developed, which, when fed with unit white noise, will output a signal with a PSD and cumulative MSV which bounds these measured PSDs and MSVs. A fitted transfer function of this shaping filter is given by

$$G(s) = a\left(\frac{b}{s+b}\right)^2 \tag{45}$$

where $a = 0.011$ is the low-frequency value of the transfer function, $b = 0.01$ rad/s is the cutoff frequency of the shaping filter, and s is the Laplace variable. The one-sided PSD of this

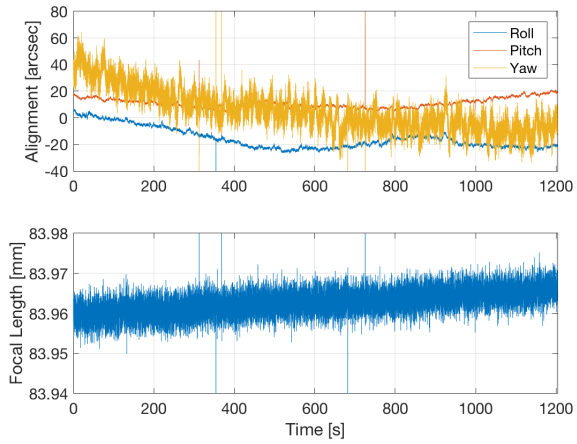

Figure 34: **Changes in the calibrated camera parameters over an observation.**

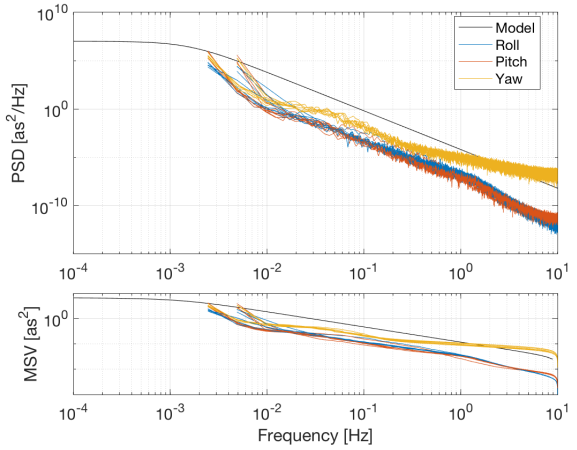

Figure 35: **Power spectral density and cumulative mean square value of star-tracker-to-payload alignment changes.**

system is given by

$$P(f) = 2\,|G(f)|^2\,, \tag{46}$$

which is plotted in Fig. 35. This resulting system, the shaping filter excited by unit white noise, can be used in either a time-domain simulation or frequency-domain analysis to determine the effect of changes in star-tracker-to-payload alignment on the overall pointing error.

5. Summary & Conclusion

This paper provided an overview of the modeling and performance of the ASTERIA payload, which is an important part of understanding the overall pointing performance of ASTERIA.

An imager model, along with laboratory measurements of key imager noise parameters, were presented. A centroiding algorithm was run on these images and compared against flight telemetry, showing that the imager model is able to predict the on-orbit centroiding performance that was achieved.

A geometric camera model was presented and used as a part of a geometric camera calibration procedure to estimate camera parameters such as focal length and alignment. On-orbit data was used to show how this calibration procedure works and how the parameters change over time, as well as create a model of the alignment changes over time.

The results of this paper will provide important information for a future publication on ASTERIA's pointing algorithms and analysis.

Acknowledgments

This work was carried out at the Jet Propulsion Laboratory, California Institute of Technology, under a contract with the National Aeronautics and Space Administration. © 2019 California Institute of Technology. Government sponsorship acknowledged. Reference herein to any specific commercial product, process, or service by trade name, trademark, manufacturer, or otherwise, does not constitute or imply its endorsement by the United States Government or the Jet Propulsion Laboratory, California Institute of Technology.

References

[1] M. W. Smith, S. Seager, C. M. Pong, J. S. Villaseñor, G. R. Ricker, D. W. Miller, M. E. Knapp, G. T. Farmer, and R. Jensen-Clem, "ExoplanetSat: Detecting transiting exoplanets using a low-cost CubeSat platform," in *Proceedings of SPIE*, J. M. Oschmann, Jr., M. C. Clampin, and H. A. MacEwen, Eds., vol. 7731 Space Telescopes and Instrumentation 2010: Optical, Infrared, and Millimeter Wave. San Diego, CA: SPIE, June-July 2010, p. 773127.

[2] C. M. Pong, S. Lim, M. W. Smith, D. W. Miller, J. S. Villaseñor, and S. Seager, "Achieving high-precision pointing on ExoplanetSat: Initial feasibility analysis," in *Proceedings of SPIE*, J. M. Oschmann, Jr., M. C. Clampin, and H. A. MacEwen, Eds., vol. 7731 Space Telescopes and Instrumentation 2010: Optical, Infrared, and Millimeter Wave. San Diego, CA: SPIE, June-July 2010, p. 77311V.

[3] C. M. Pong, M. W. Smith, M. W. Knutson, S. Lim, D. W. Miller, S. Seager, J. S. Villaseñor, and S. D. Murphy, "One-Arcsecond Line-of-Sight Pointing Control on ExoplanetSat," in *Guidance and Control 2011*, ser. Advances in the Astronautical Sciences, K. B. Miller, Ed., vol. 141, AAS. Breckenridge, CO: Univelt, Inc., February 2011, pp. 147–166.

[4] M. W. Smith, S. Seager, C. M. Pong, M. W. Knutson, D. W. Miller, T. C. Henderson, S. Lim, T. M. Brady, M. J. Matranga, and S. D. Murphy, "The ExoplanetSat Mission to Detect Transiting Exoplanets with a CubeSat Space Telescope," in *25th Annual AIAA/USU Conference on Small Satellites*, AIAA/USU. Logan, UT: Utah State University Research Foundation, August 2011, pp. 1–9.

[5] C. M. Pong, M. W. Knutson, D. W. Miller, S. Seager, S. Lim, T. C. Henderson, and S. D. Murphy, "High-Precision Pointing and Attitude Determination and Control on ExoplanetSat," in *AIAA Guidance, Navigation, and Control Conference*. Minneapolis, MN: AIAA, August 2012, pp. 1–24.

[6] M. Knapp, M. Smith, C. Pong, J. Nash, and S. Seager,

"ExoplanetSat: High Precision Photometry for Exoplanet Transit Detections in a 3U CubeSat," in *63rd International Astronautical Congress*. Naples, Italy: IAF, October 2012, pp. 1–12.

[7] C. M. Pong, S. Seager, and D. W. Miller, "Three-Degree-of-Freedom Testing of Attitude Determination and Control Algorithms on ExoplanetSat," in *Guidance and Control 2014*, ser. Advances in the Astronautical Sciences, A. J. May, Ed., vol. 151, AAS. Breckenridge, CO: Univelt, Inc., February 2014, pp. 285–307.

[8] C. M. Pong, "High-Precision Pointing and Attitude Estimation and Control Algorithms for Hardware-Constrained Spacecraft," Ph.D. dissertation, Massachusetts Institute of Technology, Cambridge, MA, June 2014.

[9] M. W. Smith, C. M. Pong, S. Lim, D. W. Miller, S. Seager, and S. D. Murphy, "Multi-Functional Star Tracker with Precision Focal Plane Position Control for Small CubeSat-Class Satellites," U.S. Patent 8,772,690 B2, July 8, 2014.

[10] M. W. Smith, A. Donner, M. Knapp, C. M. Pong, C. Smith, J. Luu, P. D. Pasquale, R. L. Bocchino Jr., B. Campuzano, J. Loveland, C. Colley, A. Babuscia, M. White, J. Krajewski, and S. Seager, "On-Orbit Results and Lessons Learned from the ASTERIA Space Telescope Mission," in *32nd Annual AIAA/USU Conference on Small Satellites*, AIAA/USU. Logan, UT: Utah State University Research Foundation, August 2018, pp. 1–20.

[11] C. M. Pong, "On-Orbit Performance & Operation of the Attitude & Pointing Control Subsystems on ASTERIA," in *32nd Annual AIAA/USU Conference on Small Satellites*, AIAA/USU. Logan, UT: Utah State University Research Foundation, August 2018, pp. 1–20.

[12] High Energy Astrophysics Science Archive Research Center, "HIPPARCOS - Hipparcos Main Catalog," http://heasarc.gsfc.nasa.gov/W3Browse/all/hipparcos.html, August 2012.

[13] J. Heikkilä and O. Silvén, "A Four-step Camera Calibration Procedure with Implicit Image Correction," in *Proceedings of IEEE Computer Society Conference on Computer Vision and Pattern Recognition*. San Juan, Puerto Rico: IEEE, June 1997, pp. 1106–1112.

[14] D. C. Brown, "Decentering Distortion of Lenses," *Photogrammetric Engineering*, vol. 32, no. 3, pp. 444–462, 1966.

[15] ——, "Close-Range Camera Calibration," *Photogrammetric Engineering*, vol. 37, no. 8, pp. 855–866, 1971.

[16] *Allen's Astrophysical Quantities*. Springer-Verlag New York, 2002.

[17] D. R. Williams, "Moon Fact Sheet," https://nssdc.gsfc.nasa.gov/planetary/factsheet/moonfact.html, July 2017.

[18] *Scientific Charge-Coupled Devices*. Bellingham, WA: SPIE Press, 2000.

[19] A. Piterman and Z. Ninkov, "Subpixel sensitivity maps for a back-illuminated charge-coupled device and the effects of nonuniform response on measurement accuracy," *Optical Engineering*, vol. 46, no. 6, pp. 1192–1202, June 2002.

[20] R. Segal, I. Shcherback, and O. Yadid-Pecht, "CMOS Image Sensors: Two-Dimensional MTF for Anisotropic Resolution Characterization," *IEEE Sensors Jornal*, vol. 7, no. 6, pp. 947–952, June 2007.

[21] C. C. Liebe, "Accuracy Performance of Star Trackers—A Tutorial," *IEEE Transactions on Aerospace and Electronic Systems*, vol. 38, no. 2, pp. 587–599, April 2002.

[22] R. Y. Tsai, "A Versatile Camera Calibration Technique for High-Accuracy 3D Machine Vision Metrology Using Off-the-Shelf TV Cameras and Lenses," *IEEE Journal of Robotics and Automation*, vol. RA-3, no. 4, pp. 323–344, August 1987.

[23] Z. Zhang, "A Flexible New Technique for Camera Calibration," *IEEE Transactions on Pattern Analysis and Machine Intelligence*, vol. 22, no. 11, pp. 1330–1334, November 2000.

[24] L. W. Fritz and H. H. Schmid, "Stellar Calibration of the Orbigon Lens," *Photogrammetric Engineering*, vol. 40, no. 1, pp. 101–115, 1974.

[25] A. Klaus, J. Bauer, K. Karner, P. Elbischger, R. Perko, and H. Bischof, "Camera Calibration from a Single Night Sky Image," in *Proceedings of the 2004 IEEE Computer Society Conference on Computer Vision and Pattern Recognition*. Washington, DC: IEEE, June-July 2004, pp. 1–7.

[26] D. Mortari, M. A. Samaan, C. Bruccoleri, and J. L. Junkins, "The Pyramid Star Identification Technique," *Navigation*, vol. 51, no. 3, pp. 171–183, Fall 2004.

BIOGRAPHY

Christopher M. Pong *received his B.S. degree in General Engineering from Harvey Mudd College in 2008, M.S. degree in Aeronautics and Astronautics from the Massachusetts Institute of Technology (MIT) in 2010, and a Sc.D. in Controls from MIT in 2014. He is currently a Guidance and Control Engineer at the Jet Propulsion Laboratory.*

Matthew W. Smith *received his B.A. in Applied Mathematics from Harvard University in 2007, M.Phil degree in Engineering from the University of Cambridge (United Kingdom) in 2009, M.S. degree in Aeronautics and Astronautics from the Massachusetts Institute of Technology (MIT) in 2010, and Ph.D. in Aeronautics and Astronautics with a focus on Space Systems from MIT in 2014. He is currently a Systems Engineer at the Jet Propulsion Laboratory.*